Development of a HUMS for UAV hybrid power system using digital twin and AI techniques

Chiara Sperlì[1], Alexander Gabriel Harej[2], Alex Mazza[3], Lucrezia Zeni[4], Giulio Angelo Guido Solero[5], Marco Giglio[6], Francesco Cadini[7]

[1,2,3,6,7]*Politecnico di Milano, Dipartimento di Meccanica, Milano, 20156, Italy*

chiara.sperli@polimi.it
alexandergabriel.harej@polimi.it
alex.mazza@polimi.it
francesco.cadini@polimi.it
marco.giglio@polimi.it

[4]*Politecnico di Milano, Dipartimento di Scienze e Tecnologie Aerospaziali, Milano, 20156, Italy*

lucrezia.zeni@mail.polimi.it

[5] *Politecnico di Milano, Dipartimento di Energia, Milano, 20156, Italy*

giulio.solero@polimi.it

ABSTRACT

Traditional aeronautical power systems, typically based on fossil fuels, present a series of limitations, including: i) the added weight associated with onboard fuel storage, ii) limited endurance due to fuel consumption, and iii) the emission of atmospheric pollutants. These constraints become particularly critical in application scenarios where extended endurance and environmental sustainability are key requirements. A notable example is represented by high-altitude, long-endurance (HALE) unmanned aerial vehicles (UAVs), whose deployment is rapidly expanding due to their suitability for a wide range of missions, including surveillance, environmental monitoring, and long-range communications. To enable the technological advancement of such platforms, alternative power generation architectures must be explored. In this context, hybrid electric power systems, integrating solar panels, lithium-ion batteries, and fuel cells, offer a promising solution. Solar and fuel cell subsystems ensure stable and continuous power generation over extended periods, including during night-time operations, while lithium-ion batteries provide high-power bursts during transient phases such as take-off, landing, or auxiliary system activation. Nevertheless, the use of these hybrid systems introduces unique challenges in terms of safety, reliability, and system complexity. They must operate in harsh environmental conditions and often require remote monitoring capabilities that enable condition-based intervention without interrupting critical missions. To address these challenges, this paper presents a Health and Usage Monitoring System (HUMS) for a hybrid power system composed of a solar panel, a lithium-ion battery, and a fuel cell, developed through the integration of digital twin modeling and artificial intelligence (AI) techniques. In particular, AI data-driven methods provide a powerful and flexible framework for monitoring the complex system composed of multiple energy sources. However, to achieve reliable performance, they require large and representative datasets, which are often unfeasible to obtain experimentally. To overcome this limitation, a digital twin of the hybrid power system is developed in the MATLAB/Simulink environment and used to simulate system behavior under both healthy and faulty conditions. The resulting synthetic data are then employed to train diagnostic/prognostic algorithms. This approach offers an efficient and scalable solution for implementing intelligent health monitoring in hybrid power systems, enhancing reliability, autonomy, and operational availability in long-endurance UAV applications.

Chiara Sperlì et al. This is an open-access article distributed under the terms of the Creative Commons Attribution 3.0 United States License, which permits unrestricted use, distribution, and reproduction in any medium, provided the original author and source are credited.

1. INTRODUCTION

Unmanned aerial vehicles (UAVs), commonly defined as drones or aircraft that operate without an onboard pilot, are extensively employed both in civil and military applications performing tasks that are unsuitable or unsafe for humans. In

the civil domain, UAVs are adopted for a wide range of purposes, including: (i) scientific research and remote sensing, (ii) forestry monitoring, (iii) rapid detection of the disaster area after earthquakes, tsunamis, and hurricanes, and (iv) seasonable inspection for the survivors in hazardous situations (Zhang, et al., 2022). In the military sector, UAVs are primarily deployed for intelligence, reconnaissance and surveillance (ISR) missions. Their role in this field has become increasingly important, largely due to their ability to carry out long-duration flights that human pilots could not sustain (Özbek, Yalin, Ekici, & Karakoc, 2020). This capability is effectively exemplified by military high altitude long endurance (HALE) UAVs, which operate at altitudes of 15–20 km and can remain airborne for periods ranging from several days to even months without the need to land. Achieving such extended endurance critically depends on the propulsion system that must combine high power density and high energy density. The former influences the maximum speed, payload capacity, operational altitude and climbing rate, while the latter directly determines the achievable flight endurance (Gang & Kwon, 2018). Traditionally, most long endurance UAVs have been powered by internal combustion engines (ICEs). Although these systems are characterized by adequate specific power and specific energy, they are also affected by several limitations, namely: (i) the need to store fuel onboard which increases the overall weight of the UAV consequently impacting its performance, (ii) the finite fuel supply, which constrains endurance since thrust generation relies on continuous fuel consumption, (iii) high emissions and a considerable environmental impact, which conflict with the growing demand for greener and more sustainable platforms, and (iv) the generation of noise and vibrations, which may compromise operational stealth and structural integrity during prolonged missions (Chen & Khaligh, 2010). To address such limitations, electrical propulsion systems have emerged as a viable alternative. The most widely adopted technologies for UAV applications include lithium-ion (Li-ion) batteries, fuel cells, and solar photovoltaic (PV) panels. Li-ion batteries are extensively used in small UAVs; however, their relatively low specific energy compared to ICEs makes them unsuitable for large UAV that require prolonged endurance. Fuel cells offer higher specific energy and generate clean power, as they operate through electrochemical reactions with water as the only by-product. Nevertheless, their use is constrained by the need to store hydrogen on board. Specifically, once the stored hydrogen is depleted, the fuel cells can no longer operate, i.e., the endurance they provide is directly determined by the available hydrogen storage capacity. Lastly, solar panels can provide continuous energy obtained through the photovoltaic effect. However, in real-world scenarios their power output is significantly influenced by environmental conditions, such as irradiance and ambient temperature variations, as well as by the UAV's orientation which affects the effective incident solar radiation. Overall, each of these electric power sources, when used individually, present intrinsic limitations that restrict their applicability. For this reason, hybrid architectures have attracted increasing attention in recent years as a means to improve the efficiency and capability of electric propulsion system in long endurance UAVs applications. These configurations integrate two or more electric power sources to compensate for the limitations of each individual technology while enhancing the overall system performance (Lee, Park, Kim, Yang, & Ahn, 2012), (Zhang, Liu, & Xu, 2016). Considering hybrid architectures based on two power sources, the most common solutions, especially for HALE UAVs, integrate Li-ion batteries with PV panels or with fuel cells. For low- and medium-altitude long-endurance UAVs, several studies have instead proposed the combination of Li-ion battery, fuel cell and PV panels as the optimal strategy to maximize UAV's endurance (Lee, Kwon, Park, & Kim, 2014), (Harvey, et al., 2012) . In these works, PV panels have been adopted as the primary energy source, supplying power mainly during the daylight phases of the mission, the battery has been employed to meet peak power demands, leveraging its fast dynamic response and high power density, whereas the fuel cells has been used as the main power source during night phases, when no irradiance was available for the PV panels. These studies have brought evidence of the effectiveness of three-component hybrid architectures in enhancing flight duration and indicate that such configurations could also represent a promising solution for HALE UAVs. Nevertheless, the practical implementation of these systems, along with their potential extension to high-altitude scenarios, still faces several challenges. One of the most critical is ensuring the safety and reliability of the propulsion system over prolonged periods and under extreme environmental conditions. Addressing this requirement calls for the development of remote monitoring strategies capable of minimizing the risk of propulsion system failures while avoiding unnecessary and costly maintenance operations. Such approach can also help prevent avoidable mission interruptions, thereby enabling more continuous and efficient UAV operations. However, designing a successful monitoring strategy for hybrid power systems is particularly challenging due to the large volume and heterogeneity of data required to assess the health of multiple power sources under varying operational conditions. In this regard, the adoption of data-driven artificial intelligence (AI) techniques, particularly deep neural networks (DNNs), represent a viable solution. In fact, in recent years, DNNs have gained much attention in health monitoring applications across various engineering domains, due to their ability to extract meaningful features from high-dimensional inputs (Khatir, et al., 2025). Despite this, DNNs based diagnostic algorithms also come with some limitations, the major of which consists in the need of a huge amount of training data. Specifically, supervised DNNs require large labeled datasets including both healthy and faulty system information and acquiring such data experimentally is often impractical because of cost constraints. In this context, the present work proposes a health and usage monitoring system

(HUMS) for UAV hybrid power systems, based on a digital twin framework combined with DNNs. The digital twin is conceived as a virtual replica of the physical power system, capable of simulating its behavior under both nominal and faulty conditions. This model enables the generation of extensive synthetic datasets that can be used to train DNNs for fault diagnosis of the power sources. The ultimate goal is to establish a preliminary version of a HUMS that can later be extended to include prognostic capabilities and real-time interaction with the physical system.

The paper is organized as follows. Section 2 presents the modeling of the hybrid power system (HPS) under nominal conditions, describes the modification introduced to model the most relevant faults affecting the three power sources, and provides a brief comparison of the simulated HPS behavior under nominal and faulty conditions. Section 3 details the adopted diagnostic framework, including a description of the training database generation, the diagnostic algorithms architectures and the DNNs training. Section 4 discusses the performance of the diagnostic algorithms during both the training and testing phases. Finally, Section 5 draws the main conclusion of the study and outlines possible future developments.

2. NUMERICAL MODELING OF THE HPS

The HPS was modeled in the MATLAB/Simulink environment, where each component of the physical system was numerically represented through dedicated blocks. The block-diagram of the complete model, reproducing the main subsystems of real architecture, is shown in Figure 1.

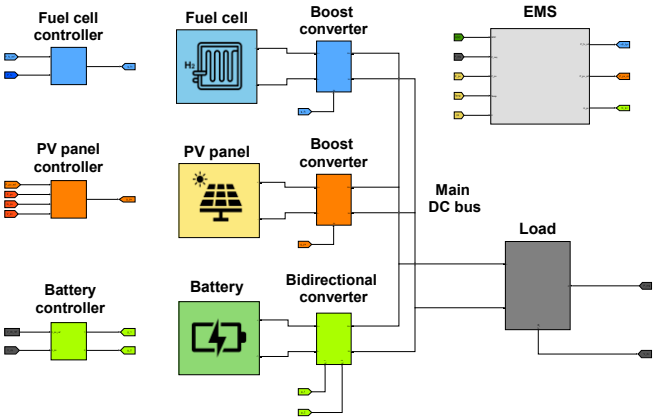

Figure 1. Schematic representation of the HPS model.

The main components of the model are the three power sources, namely the PV panel, the Li-ion battery and the fuel cell together with the onboard load and the energy management system (EMS). Each source is interfaced with the main DC bus through a dedicated DC-DC converter, and all are connected in parallel to supply the load. The EMS coordinates the operation of the sources to satisfy the instantaneous power demand, while the converters ensure proper integration with the DC bus, as the operating voltage of each source may differ from that imposed on the bus. To guarantee that the model is representative of a realistic application, the main model parameters were derived from data of commercially available items compatible with a low-speed long-endurance UAV. This UAV class was also adopted as the reference platform for defining the mission profile and the corresponding load requirements. In particular, based on data reported in the literature from flight tests of hybrid-electric UAVs of this type, the rated power during cruise was set to 200 W, whereas the maximum peak power demand during ascent was set to 1 kW. On this basis, the developed model was first employed to simulate the behavior of the HPS under nominal operating conditions of each source. Subsequently, the model was extended to include representations of the main degradation and faults affecting the individual sources. The modeling approach and the main parameters employed under both nominal and faulty conditions are described in detail in the following sections.

2.1. Modeling under nominal conditions

Each block associated with one of the power sources implements an equivalent circuit model (ECM) that reproduces the main electrical behavior of the corresponding physical component. This approach provides a simplified yet effective representation of the sources, enabling a computationally efficient system level simulation of the hybrid power system. Specifically, the Li-ion battery is represented by an ECM consisting of a controlled voltage source in series with a resistor. The resistor accounts for the internal ohmic resistance of the battery, while the value of the controlled voltage varies according to the charging and discharging conditions. This ECM formulation allows deriving a mathematical relation between the battery terminal voltage and the output current, as expressed in Eq. (1):

$$V_{batt} = f_1(it, i^*, i) - Ri \tag{1}$$

where R is the internal resistance, it is the battery's capacity, i^* is the low frequency battery dynamic, i is the battery current and the function $f_1(it, i^*, i)$ is the voltage of the controlled voltage source during discharging. This function is defined according to Eq. (2):

$$f_1(it, i^*, i) = E_0 - K\frac{Q}{Q - it} \cdot it + Aexp(-B \cdot it) \tag{2}$$

where E_0 is the constant voltage of the battery, K is the polarization constant, Q is the maximum battery capacity, A is the exponential zone amplitude, and B is the exponential capacity. During the charging phase the output voltage of the battery is evaluated as in Eq. (3):

$$V_{batt} = f_2(it, i^*, i) - Ri \tag{3}$$

where the function $f_2(it, i^*, i)$ is defined according to Eq. (4):

$$f_2(it, i^*, i) = E_0 - K\frac{Q}{it + 0.1 \cdot Q} \cdot i^* - K\frac{Q}{Q - it} \cdot it + Aexp(-B \cdot it) \quad (4)$$

The ECM used to describe the operation of the fuel cell has the same structure as that adopted for the battery, consisting of a controlled voltage source in series with a resistor. In this case, the controlled voltage source is associated with activation loss, i.e., the voltage drops due to the energy barrier that must be overcome for the electrochemical reactions to occur, while the resistor represents the ohmic loss due to the resistance to electron flow within the cell. Accordingly, the relation between the fuel cell terminal voltage and its output current is expressed by Eq. (5):

$$V_{fc} \cong E_{OC} - NAln\left(\frac{i_{fc}}{i_0}\right) - i_{fc}R_{internal} \quad (5)$$

where E_{OC} is the open circuit voltage of the fuel cell, N is the number of cells, A is the Tafel slope, i_0 is the exchange current, i_{fc} is the output current of the fuel cell and $R_{internal}$ is the internal series resistance. The PV panel is also represented through an ECM, composed of a current source, a diode, a parallel resistance and a series resistance. The current source together with the diode reproduces the behavior of the solar cell, the series resistance accounts for ohmic losses due to current transport through the semiconductor material and contacts, while the parallel resistance models leakage currents across the p–n junction and along the cell surface. According to this model, the relationship between the output current i and voltage V of the panel is given by Eq. (6):

$$i = i_L - i_0 \exp\left[\frac{qV_d}{N_{cell}nKT} - 1\right] - \frac{V + iR_S}{R_{SH}} \quad (6)$$

Where i_L is the current produced by the current source, i_0 is the cell's saturation current, q is the electron charge, N_{cell} is the number of solar cells, n is the diode ideality factor dependent on the material doping, K is the Boltzmann constant, T is the cell's temperature in unit Kelvin, V_d is the diode voltage, R_S is the series resistance and R_{SH} is the shunt resistance. The governing equations of each ECM depend on a set of quantities internally computed within the Simulink blocks on the basis of user-defined parameters. In this work, these parameters were derived from manufacturer datasheets of commercially available products taken as reference for the battery, the fuel cell and the PV panel. In particular, the Li-ion battery was modeled using data from a 25.2 V 10 Ah rechargeable pack composed of 35 cells and provided by EV lithium, the PV panel was modeled using data from SunPower A-300 solar cells arranged into three parallel strings of 52 cells each, and the fuel cell was modeled using the H-200 proton exchange membrane fuel cell (PEMFC) provided by Horizon Educational. The block of every power source is connected in series with a dedicated DC-DC converter block which is required to adapt the voltage levels of the individual sources to that of the DC bus and to regulate the power flow. Depending on the source, different converter typologies were considered: a boost converter for the fuel cell and the PV panel and a bidirectional converter for the battery, operating as a boost converter during discharge and as a buck converter during charge. Both the boost and buck converters were modeled as electrical circuits composed of an inductor, a switching device, a diode and a capacitor. Their operation depends on the switching device which is driven by a pulse-width modulation (PWM) signal that periodically opens or closes the switch. Then the duty cycle D of the PWM determines the relation between input and output voltage of the converter, as shown in Eqs. (7) and (8):

$$V_H = V_L \cdot \frac{1}{1 - D} \quad (7)$$

$$V_H = V_L \cdot D \quad (8)$$

where V_H is the input voltage while V_L is the output voltage is. Moreover, the duty cycle D is exploited to control the operating conditions of the power sources. Assuming that the main DC bus voltage remains stable over time, D is varied to modify the input voltage and consequently shifts the operating point of the power source along its characteristic curve. To implement this control, two different controllers were considered: a Proportional-Integral-Derivative (PID) power controller for the FC and a Maximum Power Point Tracking (MPPT) controller for the PV. In addition, the PV controller integrates a second control law based on the PID algorithm. This control law becomes necessary when the battery is fully charged and the power demand is lower than the maximum power that the PV can generate. In this scenario, the excess energy cannot be stored, requiring the PV power to be limited to match the power absorbed by the load. The controllers operate according to the output signals provided by the EMS. The EMS is an active, rule-based EMS based on the following principles: (i) the PV panel is prioritized as the main power source during the daytime phases of the mission, (ii) the Li-ion battery is primarily employed to compensate for sudden load variations or peak power demands, and can be recharged by the PV panel when excess energy is available, (iii) the battery state of charge (SOC) is constrained between an upper and a lower threshold, the latter being set to ensure safe landing in case both the PV panel and the fuel cell fail to supply energy, and the former to prevent overcharging, (iv) the fuel cell is designated as the main power source during nighttime phases of the mission. The pseudocode corresponding to the EMS is reported in Figure 2. The symbols used in the pseudocode are defined as follows: P_{pv}, P_{fc} and P_{bt} denote the power generated by the PV panel, the fuel and the battery, respectively; P_{req} represents the power demanded by the load; $P_{pv,max}$, $P_{fc,max}$ and $P_{bt,max}$ indicate the maximum power that can be delivered by the PV panel, the fuel and the battery, respectively; SOC_H and SOC_L correspond to the upper and lower SOC limits of the battery.

Algorithm 4 EMS Control Logic

if $SOC \geq SOC_H$ **and** $P_{req} < P_{pv,max}$ **then**
    $P_{pv} = P_{req}$
    $P_{fc} = 0$
    $P_{bt} = 0$

else if $P_{req} \geq P_{pv,max}$ **and** $SOC \geq SOC_L$ **then**
    $P_{pv} = P_{pv,max}$
    $P_{bt} = (P_{req} - P_{pv}) \cdot (SOC - SOC_L)/100$
    $P_{fc} = P_{req} - P_{pv} - P_{bt}$

else if $SOC \leq SOC_L$ **then**
    $P_{pv} = P_{pv,max}$
    $P_{fc} = \min\{(P_{pv} - P_{req} + P_{bt,max} \cdot (SOC_L - SOC)/20, P_{fc,max}\}$
    $P_{bt} = P_{req} - P_{pv} - P_{fc}$

else if $P_{req} < P_{pv,max}$ **then**
    $P_{pv} = P_{pv,max}$
    $P_{fc} = 0$
    $P_{bt} = P_{req} - P_{pv}$

end if

Figure 2. Control logic of the EMS.

The load block models a generic onboard load, which is not limited to the electric motor but may also include auxiliary devices such as cameras, sonars, and other electronic systems. In the model, these elements are represented by a variable resistor, whose resistance is dynamically adjusted according to a prescribed power profile reflecting the power demand during the UAV mission.

2.2. Modeling under faulty conditions

The numerical model of the HPS was modified to account for the main damage and degradation mechanisms affecting the three power sources. The phenomena considered were selected from faulty conditions reported in the literature according to two criteria: (i) occurrence within a time frame relevant for the UAV operational lifespan, and (ii) significant impact to the power output of the source. Based on these criteria, the modeled mechanisms are: hotspots, microcracks inside the silicon layer of a cell, and cracks in the protective glass for the PV panel, internal short circuits (ISC) and loss of lithium inventory for the battery, inlet pressures reduction, flooding and drying, and carbon monoxide (CO) poisoning for the fuel cell. The physical processes underlying these phenomena were not explicitly modeled. Instead, the Simulink blocks of each source were adapted to reproduce their equivalent effects on the electrical behavior of the system. In the case of the PV panel, the entire system was represented by two separate blocks: the first models three parallel strings with $52 - \mathrm{N_d}$ cells per string, and the second models three parallel strings with $\mathrm{N_d}$ cells per string, where $\mathrm{N_d}$ is a user-defined parameter denoting the number of damaged cells. This separation enables the reproduction of a realist condition un which only part of the panel is affected by damage, while the remaining portion operates in healthy conditions. Two bypass diodes are also connected in series with the two blocks, consistently with real PV panel design, where they are integrated to mitigate the adverse effects of faulty cells. To simulate the presence of a hotspot, the irradiance input to the block representing the damaged portion is modulated by a gain factor $\mathrm{D_1}$. Setting $\mathrm{D_1} = 0$ corresponds to complete shading of the affected cells. This representation is consistent with real operating conditions, as shading prevents the cells from generating current through the photovoltaic effect, forces them into reverse bias, and can lead to hotspot formation. Cracks in the protective glass are modeled using the same approach but $\mathrm{D_1}$ is assigned a value between 0 and 1 to represent a partial reduction of the irradiance on the damaged cells. In fact, glass cracks alter the optical properties of the glass layer and only partially reduce the irradiance reaching the silicon layer. As a result, the affected cells are not entirely unable to convert light into current, but they generate a lower current compared to undamaged cells. Microcracks in the silicon layer are modeled by introducing a parallel resistor connected to the second block. This additional resistance decreases the local shunt resistance of the affected section, simulating leakage current paths introduced by the presence of microcracks. This reflects the physical reality in which microcracks compromise the structural and electrical continuity of the silicon layer, causing localized current losses and a reduction in the effective output current. In addition to the parallel resistor, the gain factor $\mathrm{D_1}$ is also maintained in the model to reduce the effective irradiance incident on the affected cells. Although microcracks do not directly reduce the amount of light reaching the silicon layer, as would happen with macroscopic cracks or shading, their presence decreases the cell's ability to generate photocurrent. Thus, the combined effect of the parallel resistor and the adjusted irradiance models both the electrical leakage due to microcracks and the consequent reduction in current generation capacity. For the battery, the internal short circuit is simulated by introducing a parallel resistor across the terminals of the battery block. This resistor represents the low resistance pathway that forms inside the battery cell when the separator between the two electrodes is compromised. A lower short-circuit resistance results in a larger fraction of the current bypassing the external load, amplifying the effect of ISC. The loss of lithium inventory is modeled by reducing the nominal capacity parameter of the battery block. The reduction in nominal capacity is assumed to be directly proportional to the lithium loss (Gantenbein, Schönleber, Weiss, & Ivers-Tiffée, 2019). In particular, the rated capacity of the battery Q is evaluated as shown in Eq. (9):

$$Q = Q_{nom} \cdot (1 - LLI) \tag{9}$$

where Q_{nom} is the nominal capacity while LLI is expressed as the fraction of lost lithium relative to the total lithium originally present in the battery. Referring to the fuel cell, the variations in hydrogen and air inlet pressures can be caused by several factors including clogging in the piping, air filter blockage, damage to the tubing, aging of seals and joints

between supply system components, leaks and malfunctioning parts. Regardless of the cause, a partial reduction in the inlet pressures can be directly modeled by modifying the corresponding input variables of the hydrogen and air feeding pressure for the fuel cell block. With regard to flooding and drying, these phenomena act directly on the electrochemical processes within the fuel cell. Flooding occurs when water obstructs the transport of oxygen to the active catalytic sites, impairing the oxygen reduction reaction. Conversely, under drying conditions, the membrane lacks sufficient water to support effective proton (H^+) conduction. From a modeling perspective, both phenomena are equivalently represented by a series resistor to the fuel cell block. In fact, the damaged membrane and obstructed catalytic sites effectively behave as an increased resistance compared to the nominal state. Finally, CO poisoning, caused by the presence of CO in the hydrogen stream, is represented by a diode-resistor pair added in series to the fuel cell block. The diode simulates activation losses due to the slow kinetics of the electrochemical reactions on the reduced active area of the catalyst. The resistor, on the other hand, represents ohmic losses due to the presence of CO, which impedes the transport of reactants to, and removal of products from, the catalytic sites.

2.3. Simulations results

The Simulink model was adopted to simulate and analyze the behavior of the HPS during a representative mission scenario. The simulations were first performed under nominal operating conditions and subsequently repeated under faulty conditions. The mission profile was defined to replicate the basic sequence of operations of a typical UAV flight and consists of four phases: (i) warm-up and take-off, (ii) climb, with a duration corresponding to 15 minutes in real flight conditions and a maximum power demand of 1 kW, (iii) cruise, the longest mission phase, characterized by a nominal power demand of 200 W with additional power peaks of 20% of this value to mimic the temporary use of onboard systems, and (iv) descent, characterized by a reduced power demand of 160 W. The complete mission profile, together with the simulated phases, is shown in Figure 3.

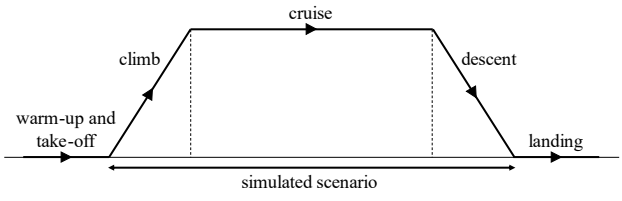

Figure 3. Schematic representation of the UAV mission profile.

The overall duration of the flight mission was set to 24 h to simulate the operation of all three power sources. Moreover, to reduce computational time, one day of real-world operation was condensed into a 3 h time window. For the sake of simplicity, the effects of latitude and weather conditions were neglected. The only environmental parameters considered were: (i) ambient temperature, fixed at 25 °C, and (ii) solar irradiance whose variations were determined based on a model of the sun's trajectory as a function of time of day and seasonal variations. In relation to the results presented in this work, equinox conditions were assumed, corresponding to 12 hours of daylight and 12 hours of darkness, with a maximum irradiance of 1000 W/m^2. Furthermore, the take-off time was set to 12 pm. The results of the simulations are summarized in Figures 4, 5, 6 and 7. Specifically, Figures 4 and 5 illustrate the power distribution among the three sources along with the power demand under nominal and faulty conditions, respectively. The main findings from Figure 4 can are as follows: (i) during take-off, both the battery and the PV panel contribute to supplying power to the load, with the battery largely compensating for the insufficient contribution of the PV panel, (ii) during the daytime cruise phase, the PV panel acts as the primary energy source and, whenever its output exceeds the load demand, the surplus power is used to recharge the battery, resulting in a negative battery power, (iii) as irradiance decreases towards zero, the PV panel power decreases as well and the fuel cell begins to supply the load, and (iv) during the night, the fuel cell operates as the main power source, with the battery assisting particularly during peak demands associated with the activation of auxiliary onboard systems. Figure 5 reports similar results, with some differences arising from the simulated presence of a glass crack in the PV panel, modeled as a 20% reduction of the incident solar irradiance and 10 damaged cells per string. This condition is considered as a representative example of anomaly in the HPS. The presence of the glass crack primarily affects the power generated by the PV panel. As shown in Figure 5, during the initial phases of the mission, the maximum PV power reaches only 400 W, which is lower than the value observed under nominal conditions. As a result, the battery is more heavily utilized, reaching a peak power of 600 W. Furthermore, due to the reduced PV output, the battery remains less charged throughout the day, which in turn leads to increased use of the fuel cell during nighttime operation. These differences can be further analyzed by examining Figures 6 and 7, which present the power profiles of each source, along with a characteristic parameter, under both nominal and faulty conditions. In general, the power delivered by the PV panel follows the solar irradiance trend, reaching its peak when irradiance is at its maximum and dropping to zero when irradiance is absent. However, under faulty conditions, it is evident that the PV panel produces less power even though solar irradiance remains unchanged. Regarding the battery, it can be observed that after the climb phase, the SOC remains around 60% under nominal conditions, while it drops to approximately 40% under faulty conditions. As previously mentioned, this results in a higher reliance on the fuel cell during the night, which is further confirmed by the hydrogen

consumption profile: in the faulty case, hydrogen consumption shows a steeper trend compared to the nominal case. Overall, the presented results also confirm the correct operation of the EMS, which effectively distributes power generation among the sources to continuously meet the power demand and successfully maintain the battery SOC within its operational limits, ranging from a lower threshold of 20% to an upper limit of approximately 90%.

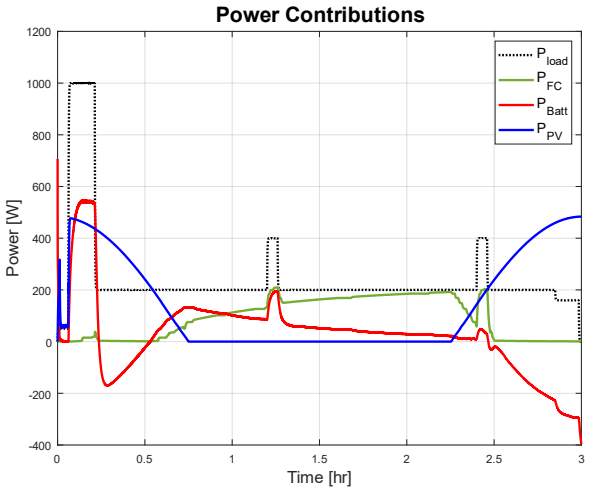

Figure 4. Power profiles of the load and the three power sources during the UAV mission under nominal conditions.

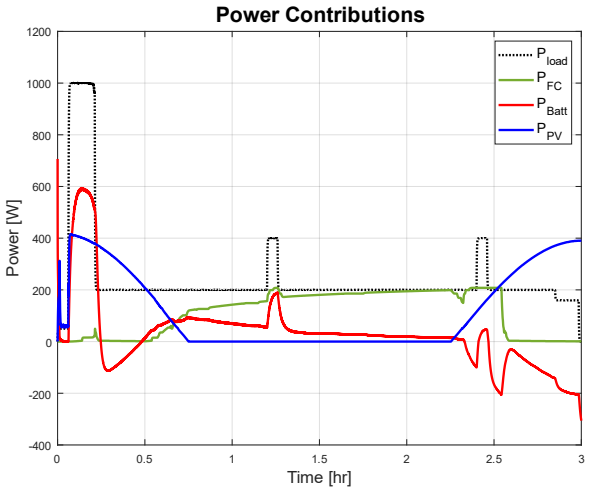

Figure 5. Power profiles of the load and the three power sources during the UAV mission under faulty conditions.

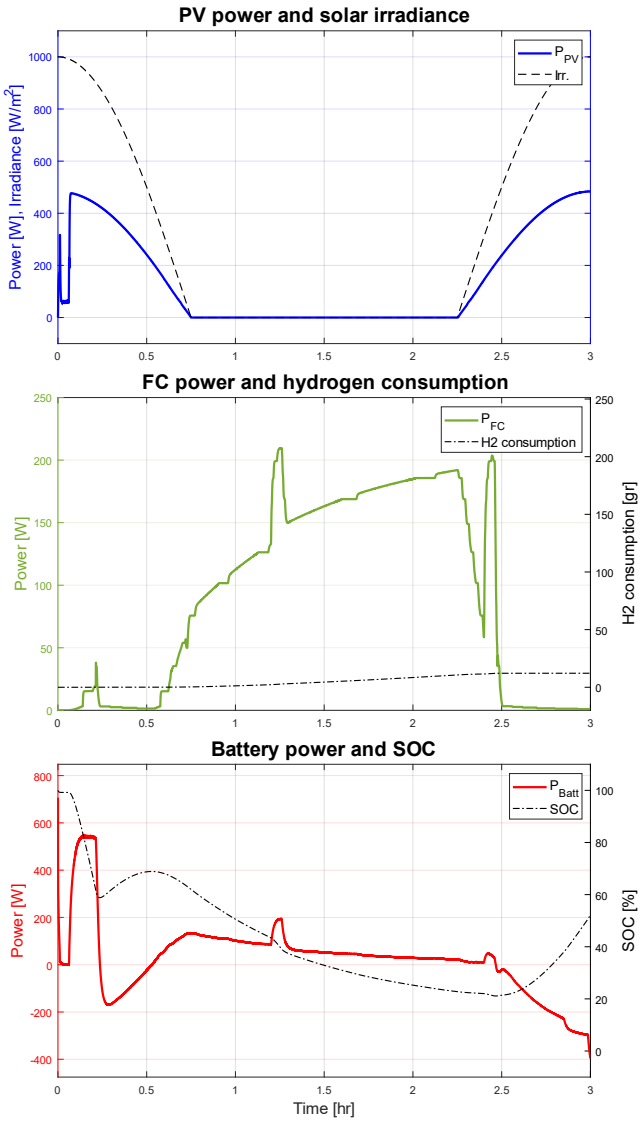

Figure 6. Power profiles and corresponding characteristic parameters of the PV panel, battery, and fuel cell during the UAV mission under nominal conditions.

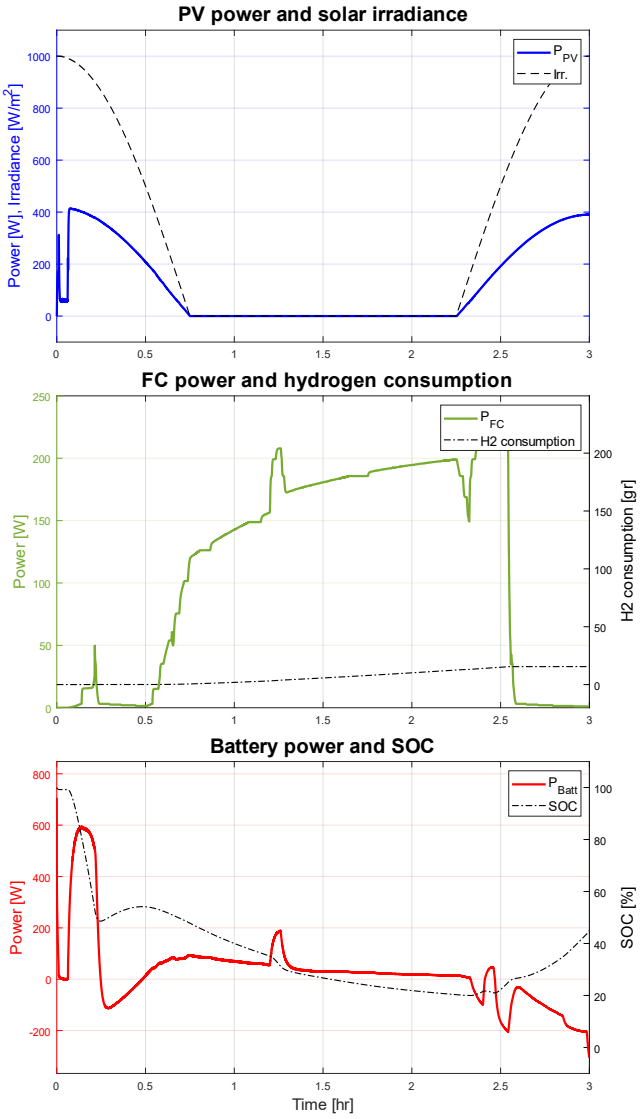

Figure 7. Power profiles and corresponding characteristic parameters of the PV panel, battery, and fuel cell during the UAV mission under faulty conditions.

3. METHODOLOGY

The numerical model of the HPS was employed to generate a comprehensive dataset of simulation signals used to train the diagnostic algorithms. This dataset was constructed by running multiple simulations under various operating scenarios, including both nominal and faulty conditions. In the case of faulty scenarios, only single fault conditions were considered, that is, each simulation involved a fault affecting only one power source at a time. This approach is based on the assumption that the simultaneous occurrence of multiple failures, either within the same source or across different sources, is less likely in realistic scenarios. The resulting signals were then used as input data for diagnostic algorithms based on deep neural networks (DNNs). Two main DNN architectures were adopted in this study: Multi-Layer Perceptrons (MLPs) and Convolutional Neural Networks (CNNs). An MLP is a type of feedforward artificial neural network consisting of an input layer, one or more hidden layers, and an output layer. Each layer is fully connected to the next, and nonlinear activation functions are applied at each hidden layer to enable the learning of complex relationships. MLPs are widely used in classification and regression tasks, and when composed of multiple hidden layers, represent one of the basic architectures in deep learning. A CNN, on the other hand, is a deep neural network architecture particularly suited for processing data with spatial or temporal structure, such as images or time series. CNNs apply learnable convolutional filters to local regions of the input, automatically extracting meaningful features. These layers are typically followed by pooling and fully connected layers. CNNs are especially effective in pattern recognition tasks and have seen broad application in a variety of areas including fault detection in time-series data. Further details regarding the generation of the training dataset and the design and implementation of the diagnostic algorithms are provided as follows.

3.1. Training database generation

The training database was constructed from signals obtained through multiple simulations of the HPS. All simulations were based on the same mission scenario described in Section 2.3, with the only varying parameter being the takeoff time, which was randomly assigned for each run. Considering the possible damage mechanisms affecting the three power sources, a total of eight faulty cases were modeled. To enrich the database and to better reflect realistic operating conditions in which damage may manifest at different severities, two severity levels were defined for each case: a partially damaged condition and a fully damaged condition. Accordingly, one simulation was performed for each damage mechanism at each severity level, resulting in a total of 16 faulty condition simulations. In addition, a further simulation was carried out to represent the healthy state of the HPS. The outcome of these simulations is a set of .csv files, each containing the time histories of key electrical and environmental signals recorded during an individual mission. Specifically, for the PV panel the selected signals include the output voltage and current, together with the irradiance applied as input to the panel block. In addition, the voltage and current at the terminals of the bypass diodes are recorded to enable discrimination among different damage types. For the fuel cell, the stack's electrical outputs are considered, namely the terminal voltage and the output current. For the battery, the monitored signals are the terminal voltage, current, and the SOC. Beyond the time histories of these signals, each .csv file also includes metadata fields reporting: (i) the model parameters used to simulate the specific damage, (ii) the mission take-off, (iii) the type of damage applied, and (iv) the severity level considered for the applied

damage. Subsequently, the signals collected into the .csv file were preprocessed before being fed into the diagnostic algorithms. Different preprocessing strategies were adopted depending on the specific power source. In particular, for the PV panel and fuel cell, a 10-second moving average sliding window was applied to each signal to attenuate high-frequency components introduced by the DC–DC converters. The mean value computed within each window was then used as the input to the DNNs, as the dynamic behavior of these sources is less critical for diagnostic purposes. A different approach was adopted for the battery, where voltage, current, and SOC were recorded as time series over 100-second intervals and then processed using a 1-second moving average sliding window on each time series. This different strategy is necessary because battery faults are primarily linked to capacity fade and altered charge–discharge dynamics, which only become evident when analysing the temporal evolution of its electrical behaviour.

3.2. DNNs based diagnostic framework

The developed diagnostic algorithms consist of deep neural networks (DNNs) designed to independently monitor the health status of each power source. Specifically, two separate neural networks (NNs) are employed for each source: (i) a regression network used for damage detection, which also accounts for varying damage severity levels, and (ii) a classification network used for damage identification, i.e., to distinguish between the different damage types considered for that source. The regression network is trained to predict a quantitative health indicator (HI) that reflects the fault severity on a continuous scale from 0 to 2, where 0 indicates a healthy state (HI = 0) and 2 represents a fully damaged state (HI = 2). Based on the predicted HI, the classification network assigns the current state to one of three predefined fault classes, represented by discrete labels ranging from 0 to 1 and associated with the different damage types. A schematic representation of this diagnostic framework, combining the two NNs, is shown in Figure 8.

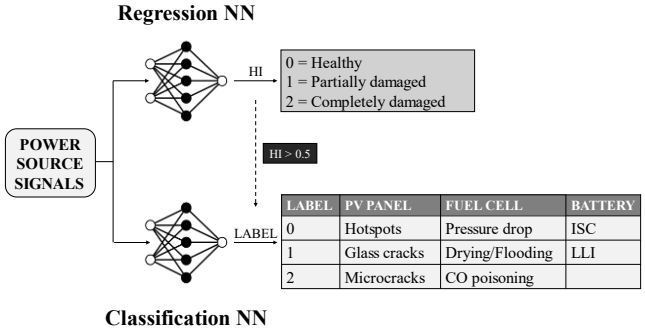

LABEL	PV PANEL	FUEL CELL	BATTERY
0	Hotspots	Pressure drop	ISC
1	Glass cracks	Drying/Flooding	LLI
2	Microcracks	CO poisoning	

Figure 8. Schematic representation of the adopted diagnostic framework.

For the PV module, the regression neural network is implemented as a MLP trained using three input signals: PV panel current, voltage, and incident irradiance. Accordingly, the input layer of the MLP consists of three neurons, one for each signal, while the output layer consists of a single neuron providing the predicted HI, normalized on a scale from 0 to 2. A similar MLP architecture is used for the classification network. However, in this case, the input set is extended to include the voltage and current of the bypass diode, resulting in a larger input layer. The output layer is also expanded to include three neurons, each corresponding to one of the predefined damage classes. Each output neuron returns the predicted probability that the input corresponds to a given damage type. These probabilities are normalized to sum to one, and the final classification result is assigned to the class with the highest probability. For the fuel cell, the NNs architectures closely mirrors those adopted for the PV panel. Specifically, an MLP regressor maps the stack voltage and current to a continuous HI, while a second MLP classifier uses the same signals to identify the fault mode. An overview of the MLP architectures adopted for the PV panel and the fuel cell is shown in Figure 9.

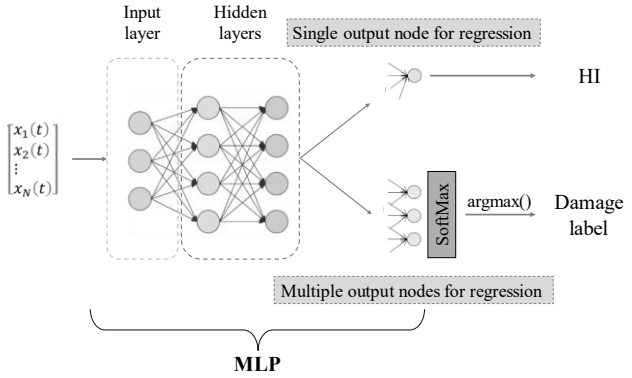

Figure 9. PV panel and fuel cell MLPs architectures.

The battery diagnostic framework follows the same two-stage approach, with one NN estimating a continuous HI and a second NN identifying the specific damage mechanism. However, unlike the PV panel and fuel cell modules, the battery networks must process sequential data to capture the temporal dynamics associated with capacity fade and charge–discharge behavior. For this reason, one-dimensional CNNs were adopted instead of MLPs. The first CNN, tasked with damage severity estimation, has an input layer that accepts a pre-processed 100×3 matrix of battery signals, where the rows represent 100 time samples within the interval and the columns correspond to voltage, current, and SOC. This input is followed by multiple consecutive convolutional layers designed to automatically learn features from the time series, and a max pooling layer that progressively reduces the temporal dimension while preserving the most relevant featurest. fully connected layers that map them into a single

continuous output. The resulting feature representation is then passed to fully connected layers that map it into a single continuous output. The final layer consists of a single neuron producing the HI. For damage mechanism identification, the same CNN architecture is employed; however, the regression output is replaced by a fully connected layer with as many neurons as fault classes, followed by a SoftMax activation to generate a probability distribution over the possible fault types. The CNN architectures described so far are illustrated in Figure 10.

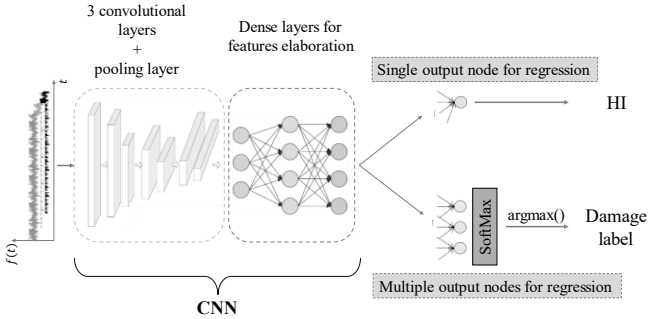

Figure 10. Battery CNN architectures.

3.3. DNNs training

The developed diagnostic algorithms were trained within a MATLAB environment, where each of the six neural networks, two per power source, was independently trained from the other. To this end, the input database was split to use the 70%, 20% and 10% of the input signal for training, validation and test, respectively. All the DNNs were trained adopting the Adam optimizer and an initial learning rate of $1e^{-3}$. During training, the learning rate was gradually reduced following a piecewise decay schedule, where it was multiplied by a factor of 0.9 every 25 epochs. Regarding the total number of epochs, a distinction was made based on the power source. The networks associated with the PV panel and fuel cell, which operate on lower-dimensional inputs, were trained for 200 epochs. Conversely, the battery networks required longer training, up to 500 epochs, to achieve accurate results on higher-dimensional inputs. Furthermore, to enhance training performance, a Bayesian optimization strategy was employed to identify the optimal set of hyperparameters. The hyperparameters considered include the number of hidden layers, the number of neurons per hidden layer, the activation function, and the mini-batch size for the MLPs of the PV panel and fuel cell. For the battery CNNs, the number of filters per convolutional layer was also included in the optimization process. Table 1 summarizes the optimized hyperparameters for all six neural networks, while Table 2 presents the corresponding loss functions. In these tables, regression NNs are denoted by the number 1, while classification NNs are denoted by the number 2.

Table 1. Summary of optimized hyperparameters.

		NN architecture	Activation function	Mini-batch size
PV	**1**	6 hidden layers, 16 neurons	Sigmoid	1028
PV	**2**	6 hidden layers, 16 neurons	Sigmoid/SoftMax	1028
FC	**1**	4 hidden layers, 50 neurons	ReLU	1028
FC	**2**	4 hidden layers, 50 neurons	ReLU/ SoftMax	1028
Batt	**1**	3 Convolutional layers (24/48/48 filters) + 6 fully connected layers (6 neurons)	ReLU	128
Batt	**2**	3 Convolutional layers (24/48/48 filters) + 6 fully connected layers (6 neurons)	ReLU/ SoftMax	128

Table 2. Training loss functions.

		Loss function
PV	**1**	Mean squared error (MSE)
PV	**2**	Categorical cross entropy loss (CCE)
FC	**1**	Mean squared error (MSE)
FC	**2**	Categorical cross entropy loss (CCE)
Batt	**1**	Mean squared error (MSE)
Batt	**2**	Categorical cross entropy loss (CCE)

4. RESULTS AND DISCUSSION

4.1. Offline diagnostic algorithms testing

The performance of the trained DNNs were evaluated on the test dataset comprising simulation signals that were not used during training or validation. For the regression networks, two standard evaluation metrics were adopted: Root Mean Square Error (RMSE) and the coefficient of determination (R^2). The RMSE provides a measure of the average magnitude of the prediction error by computing the square root of the mean squared difference between the predicted HI and the corresponding ground-truth values. A lower RMSE indicates higher prediction accuracy. The coefficient of determination quantifies how well the predicted HI values capture the variance of the true values. An R^2 of 1 indicates perfect agreement between prediction and ground truth,

whereas an R^2 of 0 implies that the model performs no better than simply predicting the mean of the dataset. The RMSE and R^2 scores obtained for each of the three regression networks are reported in Table 3.

Table 3. Performance metrics for the regression networks.

	RMSE	R^2
PV	0.049	0.996
FC	0.034	0.998
Batt	0.039	0.998

As shown in Table 3, all three regression networks achieved accurate performance on the test set. However, the PV panel model exhibited slightly lower accuracy compared to those for the fuel cell and the battery. For the classification networks, the performance of the trained DNNs were evaluated using the confusion matrices. In these matrices, each row represents the true class and each column the predicted class. An ideal classifier would produce a matrix with all values concentrated along the diagonal, indicating perfect classification. Off-diagonal entries represent misclassifications and help identify which fault modes are more frequently confused with others. The confusion matrices obtained for the classification models associated with the PV panel, the fuel cell, and the battery are shown in Figures 11, 12, and 13, respectively.

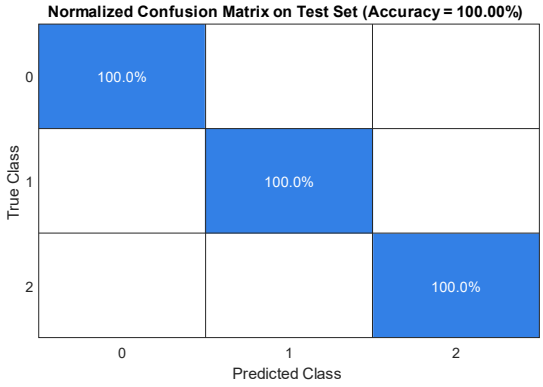

Figure 11. Confusion matrix for the PV panel classification network.

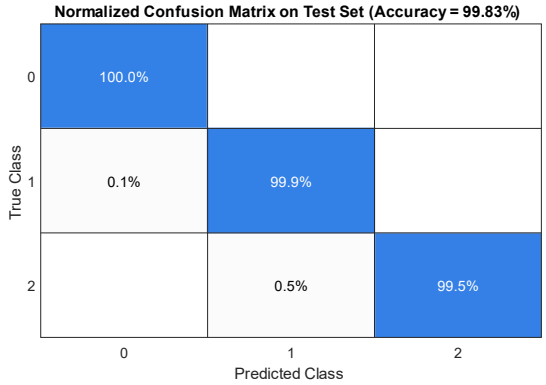

Figure 12. Confusion matrix for the fuel cell classification network.

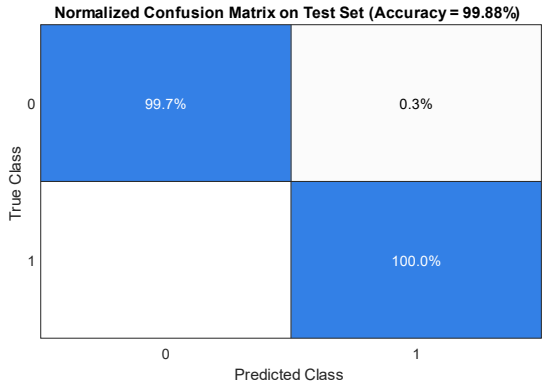

Figure 13. Confusion matrix for the battery classification network.

The confusion matrices show that the classification networks correctly identify the fault type in most cases, with only a few misclassifications observed for the fuel cell and the battery.

4.2. Real-time diagnostic algorithms testing

To further evaluate the performance of the diagnostic algorithms and assess their generalization capability, the developed DNNs were integrated into the HPS modeling environment and executed in parallel with the system simulations. This setup emulates the real-time operation of the diagnostic framework as it would occur onboard the UAV and enables the assessment of: (i) the predictive accuracy of the DNNs under realistic operating conditions, and (ii) the functionality of the entire diagnostic workflow, including the conditional activation of the DNNs and their interaction with the EMS. The latter aspect is particularly relevant for the monitoring of the PV panel and the fuel cell, which is enabled only during specific mission phases. At night, for instance, the PV panel is inactive due to the absence of sunlight, and its health monitoring is therefore suspended. Likewise, when the PV panel does not operate at its maximum power point (MPP), the characteristic curves of healthy and degraded cells tend to overlap, making it difficult to reliably discriminate

between the two conditions. For this reason, PV monitoring is activated exclusively when the panel operates at MPP and when the irradiance level exceeds 250 W/m^2. The first condition is directly obtained from the EMS control signal, while the second is retrieved from the irradiance signal. Analogously, fuel cell monitoring is enabled only when the device is operating at maximum power. This choice prevents unnecessary activation during daytime periods, when the fuel cell is not expected to operate. The proposed diagnostic framework is evaluated through two representative scenarios. The first considers a one-day flight with a fully degraded battery caused by an ISC. The second examines a two-day flight in which the fuel cell experiences progressive degradation, modeled as gradually increasing pressure drops. The corresponding real-time diagnostic results are reported in Figures 14 and 15.

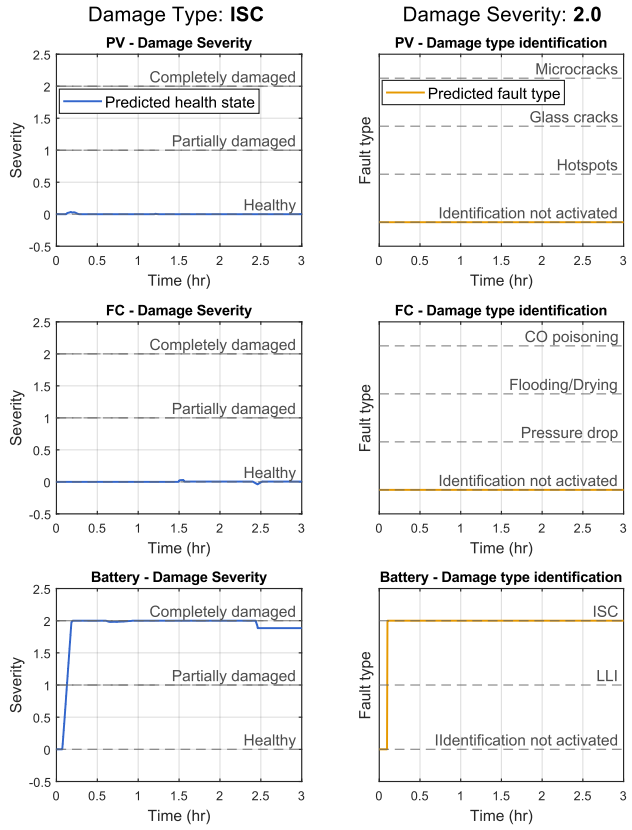

Figure 14. Results of the diagnostic algorithms for the first scenario.

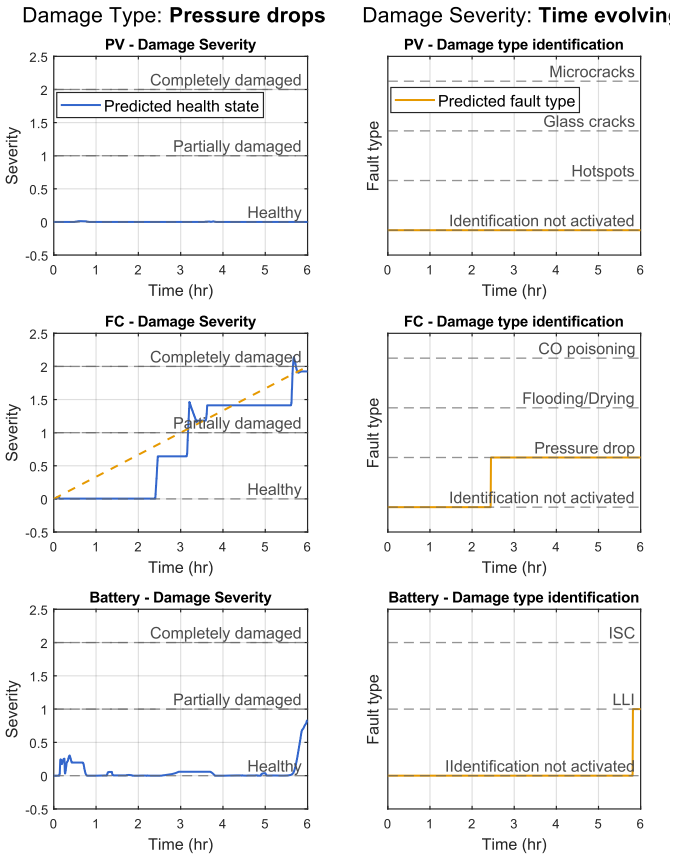

Figure 15. Results of the diagnostic algorithms for the second scenario.

The results reported in Figure 14 indicate that the regression network associated with the PV panel and the fuel cell, both operating under nominal conditions, correctly predict a HI close to zero, thereby confirming their ability to recognize healthy states and preventing unnecessary activation of the corresponding classifiers. For the battery, both regression and classification networks demonstrate the effectiveness of the framework: the fault mechanism is correctly identified from the start of the mission. Although the regression model slightly underestimates the severity in the early phase of the flight, the HI progressively converges toward the correct value as more temporal data become available. The accuracy demonstrated by the results in Figure 14 is preserved also in the more complex scenario of a time-evolving degradation affecting the fuel cell. As shown in Figure 15, both the regression and classification networks for the fuel cell correctly capture the progression of the fault, with the regression model closely following the gradual increase in severity and the classifier identifying the correct fault type throughout the mission. All other networks remain highly accurate, except for a late-mission false positive in the battery networks, classified as an ISC.

5. CONCLUSIONS

This study presented the development of a HUMS for a HPS intended for long-endurance UAV applications, integrating a digital twin framework with DNNs for fault detection and identification. The entire hybrid architecture, comprising a PV panel, a Li-ion battery, and a fuel cell coordinated by an active EMS, was modeled in the MATLAB/Simulink environment. The numerical framework was then employed to carry out multiple simulations designed to reproduce the behavior of the system under a range of operating conditions, including both nominal and faulty states of the three power sources, within a realistic UAV mission profile. The results obtained from these simulations demonstrate that the developed model can reliably capture the behavior of the hybrid power system across diverse scenarios. As such, it represents a reliable tool for generating synthetic datasets to support the training of data-driven diagnostic algorithms, thereby overcoming the limitations posed by experimental data availability. Building on this foundation, a diagnostic framework combining regression and classification DNNs was developed. The networks were trained on the synthetic data, and their performance was subsequently evaluated on an independent test dataset, both in offline and real-time conditions. In both testing scenarios, the DNNs correctly distinguished between healthy and faulty states of the three power sources, successfully tracked the evolution of fault severity, and accurately classified the underlying fault type, with only minor misclassifications. These results confirm the effectiveness of the proposed approach for monitoring UAV HPS and provide a solid basis for future developments of this work. Further studies will focus on: (i) extending the HUMS to include prognostic algorithms, thereby enabling the prediction of remaining useful life and fault progression, and (ii) developing an experimental setup of the HPS to interface the numerical model and the diagnostic/prognostic algorithms with a real laboratory-scale system. This activity is intended to validate the overall approach in a representative real-world application, ultimately establishing a complete digital twin through integration with the physical system and assessing the full HUMS under controlled experimental conditions.

REFERENCES

Chen, H., & Khaligh, A. (2010). Hybrid energy storage system for unmanned aerial vehicle (UAV). *IECON 2010-36th Annual Conference on IEEE Industrial Electronics Society*, (pp. 2851--2856).

Gang, B. G., & Kwon, S. (2018). Design of an energy management technique for high endurance unmanned aerial vehicles powered by fuel and solar cell systems. *International Journal of Hydrogen Energy*, 9787--9796.

Gantenbein, S., Schönleber, M., Weiss, M., & Ivers-Tiffée, E. (2019). Capacity fade in lithium-ion batteries and cyclic aging over various state-of-charge ranges. *Sustainability*, *11*(23), 6697.

Harvey, J. R., Jarvis, R. A., Verstraete, D., Bagg, R. L., Honnery, D., & Palmer, J. L. (2012). Development of a hybrid-electric power-system model for a small surveillance aircraft. In *28th international congress of the aeronautical sciences.*

Khatir, A., Capozucca, R., Khatir, S., Magagnini, E., Le Thanh, C., & Riahi, M. K. (2025). Advancements and emerging trends in integrating machine learning and deep learning for SHM in mechanical and civil engineering: a comprehensive review. *Journal of the Brazilian Society of Mechanical Sciences and Engineering*, 1--34.

Lee, B., Kwon, S., Park, P., & Kim, K. (2014). Active power management system for an unmanned aerial vehicle powered by solar cells, a fuel cell, and batteries. *IEEE transactions on aerospace and electronic systems*, 3167--3177.

Lee, B., Park, P., Kim, C., Yang, S., & Ahn, S. (2012). Power managements of a hybrid electric propulsion system for UAVs. *Journal of mechanical science and technology*, 2291--2299.

Özbek, E., Yalin, G., Ekici, S., & Karakoc, T. H. (2020). Evaluation of design methodology, limitations, and iterations of a hydrogen fuelled hybrid fuel cell mini UAV. *Energy*, 118757.

Zhang, C., Qiu, Y., Chen, J., Li, Y., Liu, Z., Liu, Y., . . . Hwa, C. S. (2022). A comprehensive review of electrochemical hybrid power supply systems and intelligent energy managements for unmanned aerial vehicles in public services. *Energy and AI*, 100175.

Zhang, X., Liu, L., & Xu, G. (2016). Energy management strategy of hybrid PEMFC-PV-battery propulsion system for low altitude UAVs. In *52nd AIAA/SAE/ASEE joint propulsion conference* (p. 5109).